Supplemental Information

Dissecting Sholl Analysis

into Its Functional Components

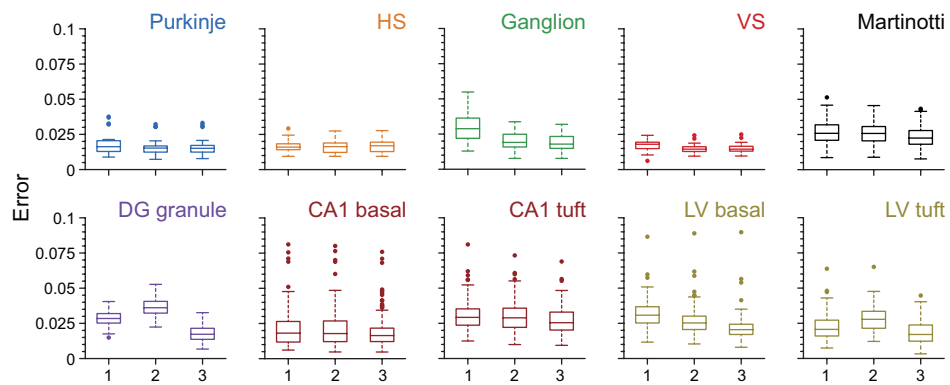**Alex D. Bird and Hermann Cuntz**

Fig S1. Related to Figure 1: Distribution of estimation errors for the different cell classes used in the paper. Errors (Eq 7) are (from left to right) in the convex domain-based prediction (Eq 1), the fitted domain-based prediction (Eq 1 with $\mathbb{D}$ defined in Methods), and the root angle based prediction (Eq 6). The number of cells of each type is given in Supplementary Table 1.
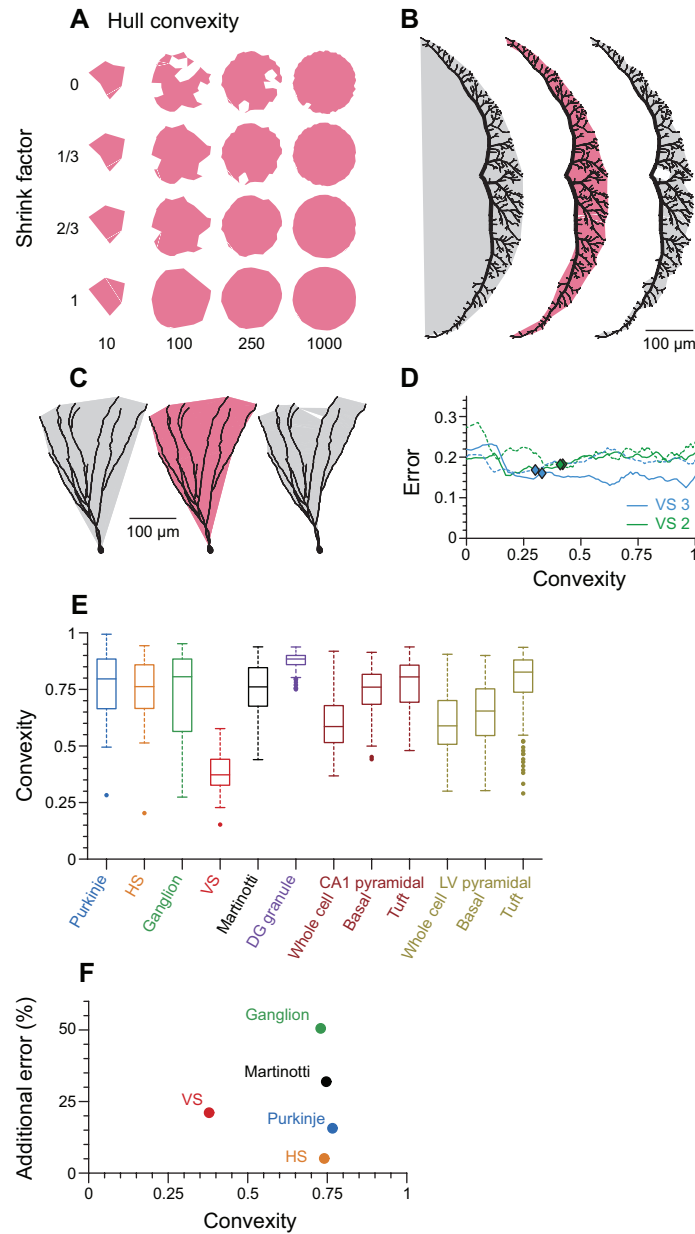
Fig S2. Related to Figure 1: Defining the dendrite spanning field for non-convex dendrites. a Illustration of different shrink factors (vertical axis) applied to sets of different numbers of points (horizontal axis) uniformly distributed in a disc in $\mathbb{R}^2$. **b** Illustration of different shrink factors (0, s∗, and 1, shaded areas) from left to right applied to a blowfly VS type 1 tangential neurons (Cuntz et al, 2008). **c** Illustration of different shrink factors (0, s∗, and 1, shaded volumes) from left to right applied to a mouse cerebellar dentate gyrus granule cell (Beining et al, 2017). **d** Error (Eq 7) in the domain-based estimation as a function of bounding shrink factor for two type 2 VS tangential cells (green lines) and two type 3 VS tangential cells (blue lines). The fitted shrink factors s∗ are shown with diamonds of the appropriate colour. **e** Distribution of convexities for different cell classes. **f** Percentage additional mean-squared error of normalised SIP (Eq 7) as a function of convexity (see Methods) for different cell classes. Higher values mean that the convex hull provides a worse boundary. The number of cells of each class is given in Table S1.
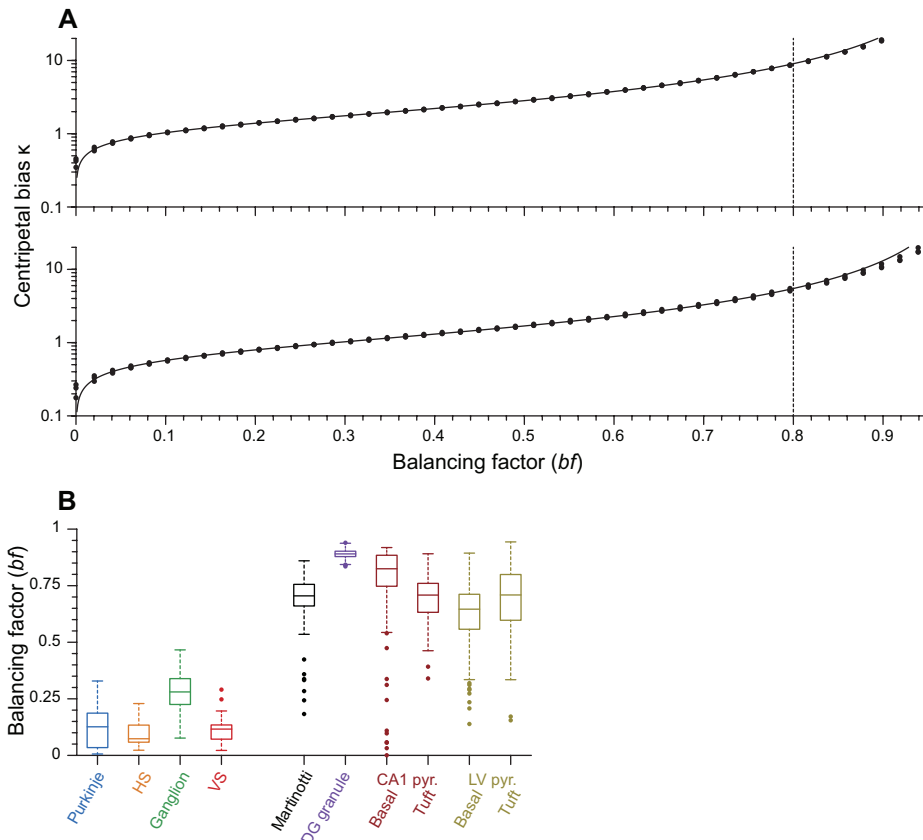
Fig S3. Related to Figure 3: Relating balancing factor bf **to centripetal bias** κ**. a** Centripetal bias κ as a function of balancing factor bf for different shapes in $\mathbb{R}^2$ (top) and $\mathbb{R}^3$ (bottom). Numerical results are given as black shapes (circles, squares, and triangles correspond respectively to circular, square, and triangular boundaries in $\mathbb{R}^2$ and to spherical, cubic, and conical boundaries in $\mathbb{R}^3$); the fits under Eq 10 are given by the solid line with parameters described in Methods. **b** Distributions of balancing factors bf for different cell classes estimated from the root angle distribution. The number of cells of each class is given in Table S1.
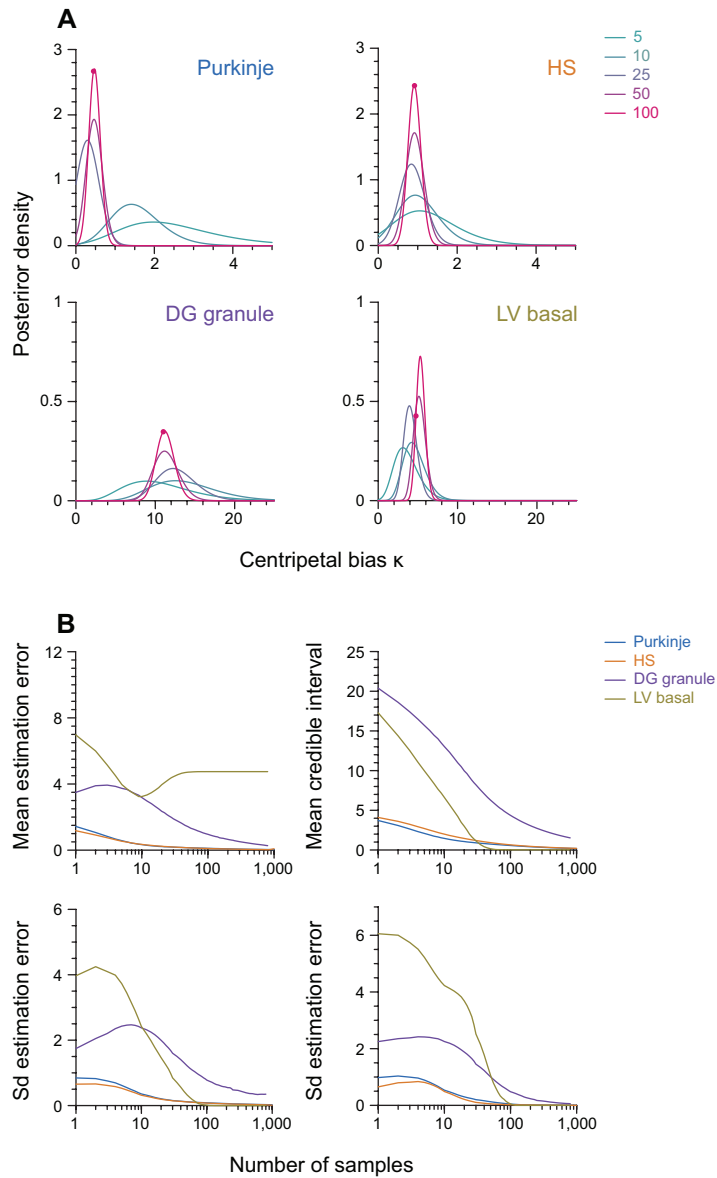
Fig S4. Related to Figure 3: Inferring centripetal bias. a Example posterior distributions for the centripetal bias parameter κ after different numbers of independent samples from reconstructed dendrites. Clockwise from top left the dendrites are a cerebellar Purkinje cell, a tangential HS cell, the basal dendrites of a cortical layer V pyramidal cell, and a dentate gyrus granule cell. The maximum likelihood estimate of κ from the entire cell is indicated in each panel by a dot on the 100 sample posterior distribution. **b** Top left: The mean estimation error for κ as a function of the number of samples. Bottom left: The standard deviation in estimation error for κ as a function of the number of samples. Top right: Width of the 95% credible interval for κ as a function of the number of samples. Bottom right: The standard deviation in the width of the 95% credible interval for κ as a function of the number of samples. Each plot shows the values for an example cell of each of the four types above

Fig S5. Related to Figure 5: Automated sorting of pyramidal cells into basal, apical trunk and apical tuft regions. Selection of 3 hippocampal CA1 (left) and three cortical Layer V (right) pyramidal cells sorted into basal and apical tuft segments (shaded purple). All dendritic radii increased by 1μm for visualisation purposes.
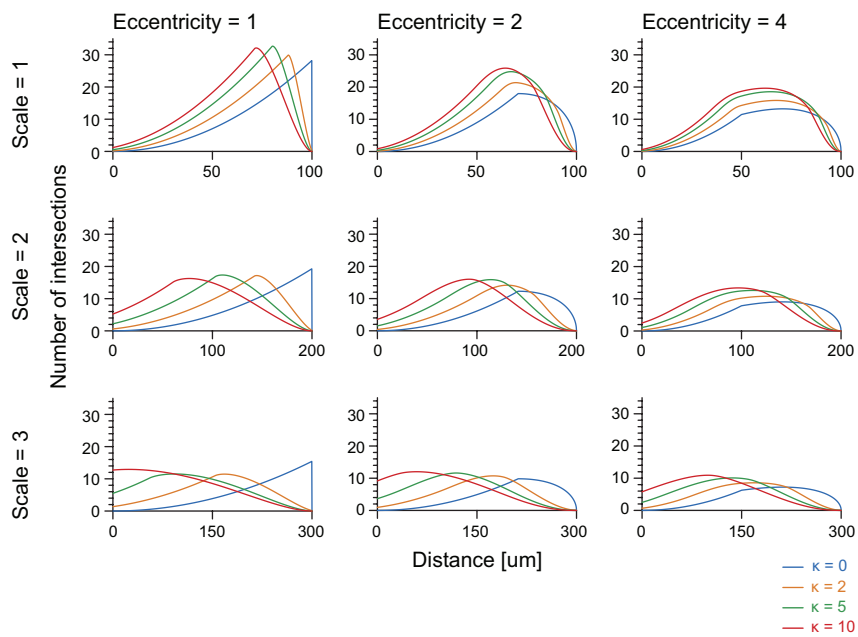

Fig S6. Related to Figure 6: Analytical form of SIP for an idealised domain. Analytical SIPs under Eqs 15 and 16. The domain $\mathbb{D}$ is taken to be a sphere of radius 100μm, which is scaled up in each dimension by the Scale (vertical direction) and flattened by the Eccentricity into an ellipsoid along one axis (horizontal direction). For each domain, four different values of centripetal bias κ (0, 2, 5, and 10) are plotted. The density of dendrite is proportional to the volume of the domain to the power -0.55 (see text), and the integral of the SIP follows from Eq 6.

Cell class	Number of cells studied	Convexity	Centripetal bias κ	R^2 value
Cerebellar purkinje	28	0.77 ± 0.17	**0.87** (0.73, 1.00)	0.91
Retinal ganglion	31	0.74 ± 0.16	**0.89** (0.72, 1.06)	0.87
HS	25	0.73 ± 0.19	**1.49** (1.36, 1.62)	0.97
VS	30	0.38 ± 0.10	**0.96** (0.74, 1.17)	0.83
Cortical LV Martinotti	175	0.75 ± 0.11	**3.25** (2.86, 3.64)	0.93
Dentate gyrus granule	242	0.87 ± 0.03	**12.07** (11.29, 12.86)	0.99
Hippocampal CA1 (basal)	161	0.74 ± 0.10	**7.39** (5.89, 8.88)	0.80
Hippocampal CA1 (tuft)	161	0.76 ± 0.13	**3.51** (2.89, 4.13)	0.84
Cortical LV pyramidal (basal)	167	0.65 ± 0.13	**2.69** (2.26, 3.12)	0.86
Cortical LV pyramidal (tuft)	167	0.78 ± 0.14	**3.24** (2.42, 4.07)	0.84

Table S1. Related to Figures 1 to 5. Table of numbers of morphologies of each cell class in the study, with the mean ($\pm$ standard deviation) of the convexity, fitted centripetal biases κ with 95% confidence intervals, and R^2 values for the von Mises model fits.

Figure	Panel	Provenance
	a	Rat cerebellar Purkinje cell NMO_00891 (Vetter et al, 2001).
	b	Guinea pig cerebellar Purkinje cell NMO_00611 (Rapp et al, 1994).
	c	Blowfly *Calliphora Vicina* HS visual neuron NMO_06656; published with the Trees Toolbox (Cuntz et al, 2008).
Figure 1	d	Rabbit retinal local projecting ganglion cell NMO_62508 (Guo et al, 2013).
	e	Blowfly *Calliphora Vicina* VS visual neuron NMO_06661; published with the Trees Toolbox (Cuntz et al, 2008).
	f	Blowfly *Calliphora Vicina* VS visual neuron NMO_06671; published with the Trees Toolbox (Cuntz et al, 2008).
	g	Mouse cortical Layer V Martinotti interneuron NMO_60397 (Castillo-Gómez et al, 2015).
	a	Rabbit retinal starburst amacrine cell NMO_00765 (Bloomfield and Miller, 1986).
Figure 2	b	Rat cerebellar Purkinje cell NMO_00891 (Vetter et al, 2001).
	c	Rat hippocampal dentate gyrus granule cell NMO_50707 (Beining et al, 2017).
	a	Rat hippocampal dentate gyrus granule cell NMO_50707 (Beining et al, 2017).
Figure 3	d	Rat cerebellar Purkinje cell NMO_00891 (Vetter et al, 2001), blowfly *Calliphora Vicina* HS visual neuron NMO_06656; published with the Trees Toolbox (Cuntz et al, 2008), dentate gyrus granule cell as above, and rat hippocampal CA1 pyramidal cell NMO_08608 (Marcelin et al, 2012).
	b	Rat neocortical Layer V pyramidal cell available on ModelDB with Accession no. 13953 (first morphology, Hay et al (2011)).
Figure 5	c	Rat hippocampal dentate gyrus granule cell NMO_50707 (Beining et al, 2017).
	d	Rat hippocampal CA1 pyramidal cell NMO_08608 (Marcelin et al, 2012).
	a	Blowfly *Calliphora Vicina* HS lobula plate tangential neuron NMO_06656 (published with the Trees Toolbox, Cuntz et al (2008)) and fruitfly *Drosophila Melanogaster* lobula plate tangential HS neuron NMO_50994 (Cuntz et al, 2013).
Figure 6	b	Mouse hippocampal dentate gyrus granule cells with and without perforant path lesion, morphologies from Vuksic et al (2011).
	c	Mouse hippocampal CA1 pyramidal neurons, wild type and in a transgenic model of Alzheimer's disease, morphologies from Šišková et al (2014).

Table S2. Related to all Figures. Table of morphologies shown in each figure in the paper. Where morphologies are downloaded from NeuroMorpho (Ascoli et al, 2007), IDs are provided, otherwise the provenance is described.